A Squall-Line-Like Principal Rainband in Typhoon Hagupit (2008) Observed by Airborne Doppler Radar

XIAOWEN TANG

Key Laboratory for Mesoscale Severe Weather/MOE, and School of Atmospheric Sciences, Nanjing University, Nanjing, China

WEN-CHAU LEE

National Center for Atmospheric Research, Boulder, Colorado

MICHAEL BELL

University of Hawai'i at Mānoa, Honolulu, Hawaii

(Manuscript received 22 September 2013, in final form 14 March 2014)

ABSTRACT

This study examines the structure and dynamics of Typhoon Hagupit's (2008) principal rainband using airborne radar and dropsonde observations. The convection in Hagupit's principal rainband was organized into a well-defined line with trailing stratiform precipitation on the inner side. Individual convective cells had intense updrafts and downdrafts and were aligned in a wavelike pattern along the line. The line-averaged vertical cross section possessed a slightly inward-tilting convective core and two branches of low-level inflow feeding the convection. The result of a thermodynamic retrieval showed a pronounced cold pool behind the convective line. The horizontal and vertical structures of this principal rainband show characteristics that are different than the existing conceptual model and are more similar to squall lines and outer rainbands.

The unique convective structure of Hagupit's principal rainband was associated with veering low-level vertical wind shear and large convective instability in the environment. A quantitative assessment of the cold pool strength showed that it was quasi balanced with that of the low-level vertical wind shear. The balanced state and the structural characteristics of convection in Hagupit's principal rainband were dynamically consistent with the theory of cold pool dynamics widely applied to strong and long-lived squall lines. The analyses suggest that cold pool dynamics played a role in determining the principal rainband structure in addition to storm-scale vortex dynamics.

1. Introduction

The spiral rainband is one of the most identifiable components of a tropical cyclone (TC). They comprise most of the precipitation outside the eyewall and exhibit great variation in structure and evolution. Willoughby et al. (1984) first categorized different TC rainbands (TCRs) as either moving or quasi-steady rainbands. The quasi-steady rainbands consisted of three different types: the principal rainband, secondary rainbands, and the connecting rainband. The principal rainband is the most predominant rainband in a TC and is hypothesized to exist on the boundary between the vortex circulation and the environmental flow (Willoughby et al. 1984; Willoughby 1988; Houze 2010). Wang (2009) further quantified this vortex–environment boundary as approximately 3 times the radius of maximum wind (RMW) and categorized TCRs as inner rainbands if their radial locations were inside this boundary, or outer rainbands conversely. Recent studies have shown distinct differences in structures between inner and outer rainbands (Houze 2010; Li and Wang 2012), with the convection in inner rainbands more vertically confined with outward-tilting convective cores (Didlake and Houze 2013a) and the convection in outer rainbands more vertically developed with inward-tilting convective cores (Yu and Tsai 2013). Although much of the TCR structure is determined by the radial location from the vortex center and associated change in rotational dynamics, there can

Corresponding author address: Wen-Chau Lee, National Center for Atmospheric Research, 3450 Mitchell Lane, Boulder, CO 80301.
E-mail: wenchau@ucar.edu

be significant azimuthal variation as well. If the convective forcing is asymmetric, then convectively active cells mature as they move downstream azimuthally and transition to stratiform precipitation. The transition plays an important dynamic role as it changes the convergence and associated vortex stretching from low to midlevels (Didlake and Houze 2013b).

Because of its predominance and persistence, the principal rainband is probably the most documented rainband type in the literature (e.g., Barnes et al. 1983; Powell 1990; May 1996; Hence and Houze 2008). Barnes et al. (1983, their Fig. 18a) proposed a conceptual model of the mesoscale and convective-scale circulations across the principal rainband of Hurricane Floyd (1981), which features an overturning updraft originated in the inflow layer and a descending downdraft from the midlevel. Hence and Houze (2008, their Fig. 13b) verified and revised the aforementioned conceptual model of a principal rainband by deducing similar convective-scale flow patterns using high-resolution airborne dual-Doppler observations. These previously studied principal rainbands all possessed inner rainband characteristics with limited vertical extent and outward-tilting convective cores. These structural characteristics indicate that the principal rainband is strongly constrained by vortex dynamics and therefore may be more appropriately considered as the inner TCR (Yu and Tsai 2013). Nevertheless, since the principal rainband is hypothesized to manifest near the vortex–environment boundary, certain parts of the principal rainband can indeed be outside of the inner-core region and have similar vertical structure to that of outer rainbands (Houze 2010). Because of the limited observations, the connection between the principal rainband and outer rainbands in terms of their structure and dynamics remains poorly understood (Yu and Tsai 2013).

Outer rainbands are located radially far away from the inner-core region and are relatively unconstrained by vortex dynamics. The structure of outer rainbands appears to be dominated by buoyancy and has more intense convection (Houze 2010; Yu and Tsai 2013) owing to the availability of larger convective available potential energy (CAPE) (Bogner et al. 2000; Molinari et al. 2012). With the increased intensity of convection in outer rainbands and the drier midlevel air in the environment (Eastin et al. 2012; Yu and Tsai 2013), the cooling effect in the stratiform region seems to become important. Significant and widespread surface cold pools with a local temperature decrease of 1–4 K have been documented alongside outer TCRs using surface stations (Skwira et al. 2005; Yu and Tsai 2010; Yu and Chen 2011; Eastin et al. 2012). Using idealized numerical simulation, Sawada and Iwasaki (2010) demonstrated

the existence of significant cold pools associated with TCRs generated by evaporative cooling from raindrops. The existence of widespread surface cold pools associated with TCRs, especially outer TCRs, indicates that they may play a dynamic role in determining different TCR structures.

The dynamics associated with cold pools have been shown to play a decisive role in modulating the structure and evolution of squall lines in the midlatitudes (Rotunno et al. 1988, hereafter RKW; Weisman and Rotunno 2004). The basic mechanism of cold pool dynamics can be understood by assessing the relative strength of convectively generated surface cold pool and low-level environmental vertical wind shear (VWS). When these two factors are quasi balanced, they can counteract each other and lead to the strongest lifting of environmental air. This quasi-balanced state is often referred to as the "optimal state" (RKW). Because of the distinct thermodynamic structure in the TC context (Sheets 1969; Bogner et al. 2000) from that in the midlatitudes (Bluestein and Jain 1985; Bluestein et al. 1987), the potential role of cold pool dynamics on the structure and evolution of TCRs has not yet been fully understood. Barnes et al. (1991) investigated the relative magnitude of low-level VWS and conditional instability and showed that the buoyancy dominated environment matches the observed convective structure with the characteristics of ordinary cells. Yu and Tsai (2013) examined the low-level environmental VWS and cold pool strength associated with outer TCRs and showed that the observed convective structure was consistent with the theory of cold pool dynamics. While abovementioned studies suggest the potential role of cold pool dynamics in modulating TCR structure, further study is required to understand the extent of its impact to different TCRs.

In this paper, the mesoscale and convective-scale structures of Typhoon Hagupit's principal rainband observed during The Observing System Research and Predictability Experiment (THORPEX) Pacific Asian Regional Campaign (T-PARC) and Tropical Cyclone Structure 2008 (TCS-08) experiment (Elsberry and Harr 2008) are presented using airborne dual-Doppler radar analyses. This study is intended to contribute to the ongoing studies (Hence and Houze 2008; Didlake and Houze 2009; Li and Wang 2012; Didlake and Houze 2013a,b; Yu and Tsai 2013) of understanding the characteristic structure of different TCRs and their underlying dynamics. Hagupit's principal rainband consisted of deep and intense convective elements organized into a linear pattern, and the overall line-averaged vertical structures were distinct from those of previously documented inner and outer TCRs. The environment of the
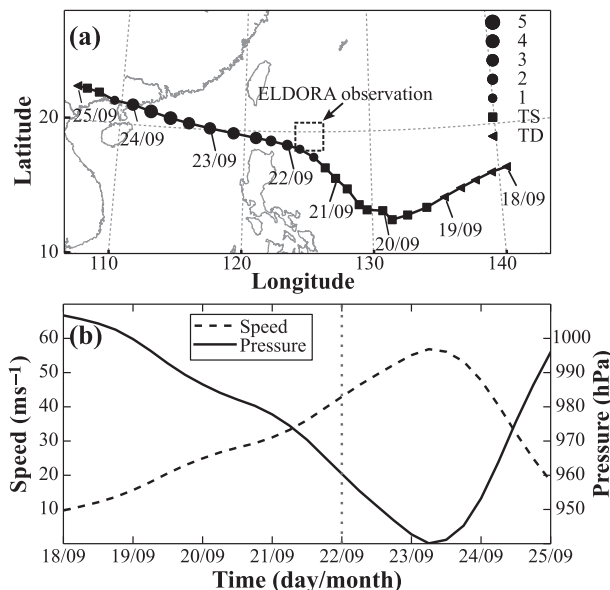
FIG. 1. The (a) best track and (b) intensity of Typhoon Hagupit (2008).

convective line was characterized by veering low-level VWS perpendicular to the line and large CAPE value. A pronounced cold pool was located in the stratiform region radially inside the intense convective line, and its strength was approximately balanced with that of the low-level VWS. The kinematic and thermodynamic structures of the convective line are consistent with those of strong and long-lived squall lines in the optimal state. This study provides the first observational evidence that the principal rainband can have similar structures to those of outer TCRs, and the cold pool dynamics may play an important role in modulating the convective-scale structure of principal rainbands in addition to storm-scale vortex dynamics.

2. Storm history and aircraft mission

Typhoon Hagupit was the fourteenth tropical storm in the northwestern Pacific Ocean in 2008. Figure 1a shows its best track using the dataset from Joint Typhoon Warning Center (JTWC). Hagupit was first declared a tropical depression in the northeast of Guam on 14 September 2008 after a period of organization as an easterly wave (Bell and Montgomery 2010). During the following 5 days, it moved west-southwest and slowly developed into a tropical storm. Within a day after obtaining tropical storm intensity, Hagupit changed its course and headed northwest. An intensifying period occurred after this recurvature, and Hagupit reached category-4 intensity (Simpson et al. 2003) on 23 September right

before its landfall in the Guangdong province of China. Figure 1b shows the temporal evolution of sustained surface maximum wind and minimum central pressure a week before Hagupit's landfall. The vertical dotted line marks the starting time of the airborne radar observation, which corresponds to the intensifying phase of Hagupit. The sustained surface maximum wind speed reached approximately $46 \, \mathrm{m \, s^{-1}}$, and the minimum central pressure fell below 960 hPa.

The rainband of Typhoon Hagupit examined in this study was observed in one research flight during the T-PARC/TCS-08 field campaign. The T-PARC/TCS-08 field campaign was an international effort to observe, understand, and predict the potential impacts of TCs in the western North Pacific. One highlight of this field campaign was the use of multiplatform airborne observations—including airborne radar on board a U.S. Naval Research Laboratory (NRL) P-3, dropsondes deployed by the NRL P-3, U.S. Air Force C-130, and the Astra jet from the Dropwindsonde Observations for Typhoon Surveillance near the Taiwan Region (DOTSTAR; Wu et al. 2005), and lidars on board the NRL P-3 and a Falcon 20 jet (Chou et al. 2011)—to extensively observe the kinematic and thermodynamic structure of TCs. Since there are no routine airborne radar observations over the western North Pacific, the coordinated observation of multiple aircrafts provided an unprecedented dataset to understand the structure and dynamics of TCs over the western North Pacific. The dashed box overlaid on Fig. 1a highlights the area of this flight mission during 0010–0510 UTC 22 September 2008. It is noted that the observation area is over the open ocean that is uncompromised by any landmass. During the 5 h of aircraft flight mission, the National Science Foundation (NSF)/National Center for Atmospheric Research (NCAR) Electra Doppler Radar (ELDORA) on board the NRL P-3 aircraft repeatedly observed the most predominant rainband of Hagupit (Fig. 3d) and collected four sets of dual-Doppler observations along quasi-straight flight tracks. The DOTSTAR Astra jet started to deploy dropsondes, targeting the entire storm, about 3 h before the mission of ELDORA. Figure 2 shows the flight tracks of both aircrafts and the locations of dropsondes deployed by DOTSTAR. The flight tracks of the two aircrafts were closest during the first quasi-straight flight leg (thick dashed line) of the NRL P-3 (0010–0110 UTC), and the DOTSTAR dropsonde deployed at 0012 UTC is most adjacent to the observed rainband in terms of both time and space. Since all four sets of dual-Doppler observations showed consistent TCR structures, only the result from the first flight leg is discussed in this paper.
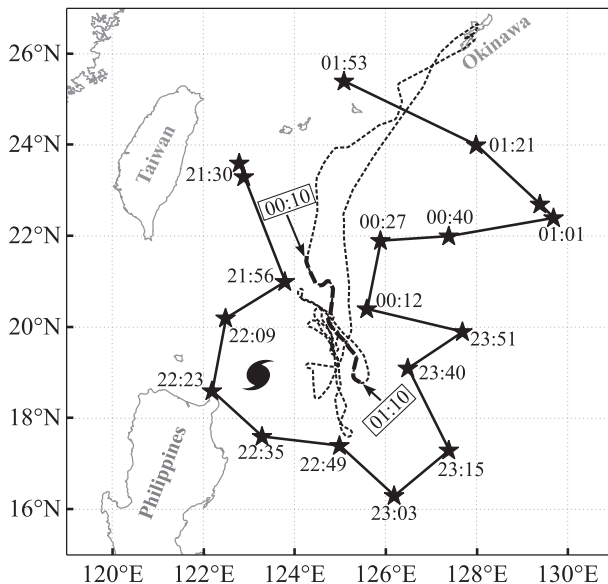
FIG. 2. The flight tracks of the NRL P-3 (dashed) and the Astra jet (solid). The stars denote the locations of dropsondes deployed by the Astra jet targeting Typhoon Hagupit. The thicker section of the NRL P-3's flight track highlights the first flight leg. The TC icon shows the storm center of Hagupit at 0040 UTC 22 Sep 2008.

3. Data and methodology

The main dataset used in this study is dual-Doppler radar observations collected by the NSF/NCAR ELDORA. ELDORA is an innovative radar system specially designed for the observation of atmosphere storms (Hildebrand et al. 1996). It features two back-to-back-mounted antennas scanning simultaneously, which are capable of collecting dual-Doppler observation with 0.4-km resolution along the flight track and 0.15-km resolution along the radar beam. This high-resolution airborne radar system has been widely used in recent studies focusing on convective-scale structures (Houze et al. 2007; Hence and Houze 2008; Didlake and Houze 2009; Houze et al. 2009; Bell and Montgomery 2010; Didlake and Houze 2013a,b). Dropsonde observations released from the Astra jet and the NRL P-3 are used to examine the environmental thermodynamic and kinematic structures associated with the observed rainband. The two aircrafts flew at different altitudes, and the dropsondes from the Astra jet and NRL P-3 were released from 10- and 3-km height, respectively. The DOTSTAR dropsonde is important to this study because it sampled the environmental kinematic and thermodynamic structures throughout most of the troposphere.

The airborne radar observation period analyzed here was from 0010 to 0110 UTC 22 September 2008. To compensate for the beam-pointing error and the

uncertainties in the aircraft altitudes derived from the Inertial Navigation System (INS), the ELDORA observations were first corrected for navigation error using techniques described by Testud et al. (1995) and Bosart et al. (2002). The ELDORA data were then processed via automated data quality control scripts (Bell et al. 2013) in the NCAR Soloii software (Oye et al. 1995) to remove nonmeteorological artifacts such as ocean surface, second-trip surface returns, sidelobe echoes, and other noise. Manual editing in the NCAR Soloii was performed to clean up remaining artifacts after the aforementioned batch processes.

The quality-controlled radar data were then interpolated into a three-dimensional Cartesian grid using an exponential weighting function with radius of influence of 1.0 km. The spatial resolution of the Cartesian grid is 0.5 km in both horizontal and vertical directions. A variational algorithm (Gamache 1997) was used to combine observations from two radars and the mass continuity equation to solve for the three-dimensional wind field. This variational algorithm has been widely used in airborne radar data synthesis (Reasor et al. 2000, 2009; Rogers et al. 2012). Further details on the formulation of this variational scheme can be found in appendix A of Reasor et al. (2009). The retrieved three-dimensional wind field was postprocessed with the three-step Leise filter (Leise 1981) to remove possible aliasing from unresolved scale features. Convective features with spatial wavelength larger than 4 km are preserved in this analysis, which is adequate for many convective features. The filtered three-dimensional wind field was further used in a set of momentum and thermodynamic equations to retrieve pressure and temperature perturbations in the convective region (Roux et al. 1993). The following analyses are conducted in a storm-relative coordinate with the storm motion removed from the retrieved wind field. The storm motion was estimated to be approximately $6.8 \, \mathrm{m \, s^{-1}}$ toward 330° during the time of airborne radar observation based on the best-track data. As shown in Fig. 1a, Typhoon Hagupit headed steadily in a north-northwest direction during the aircraft mission. The estimated storm motion is likely representative of the average motion over this time period.

4. Principal rainband of Typhoon Hagupit

Figure 3 shows four microwave images around 0000 UTC 22 September 2008 from the Defense Meteorological Satellite Program (DMSP) and Tropical Rainfall Measuring Mission (TRMM). These images show the brightness temperature at the 85(91)-GHz channels, which are sensitive to large hydrometeors mainly generated by deep convection (Spencer et al. 1989). Because of
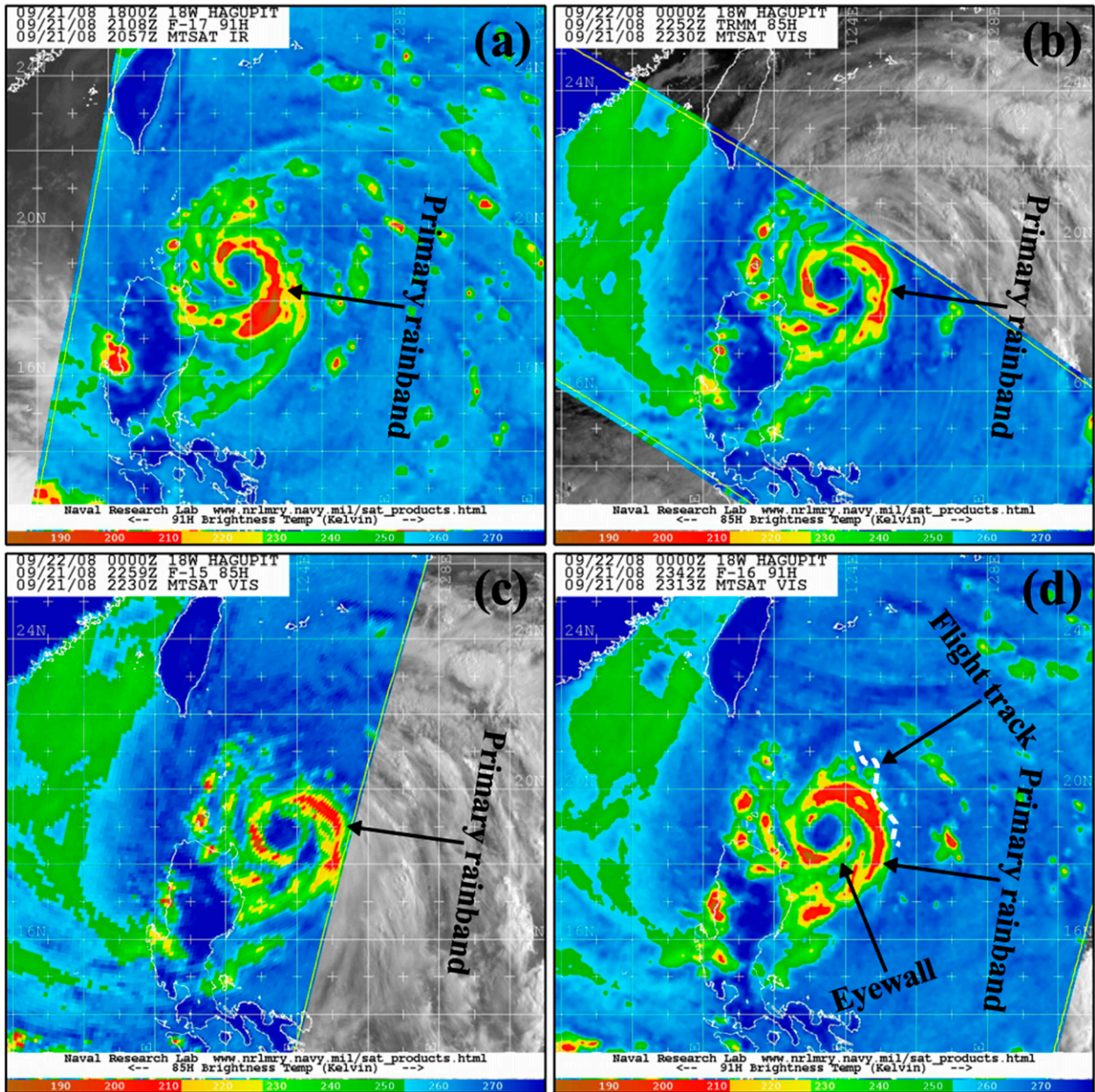
FIG. 3. Storm structure of Typhoon Hagupit and its principal rainband revealed by four microwave satellite images within about 3 h ahead of the flight mission. (d) The white dashed line shows the flight track (flying from top to bottom) of the NRL P-3.

its relative transparency to cirrus cloud, the microwave imagery near the 85-GHz channel are commonly used to reveal the structure of the eyewall and the organization of the spiral bands in TCs (Lee et al. 2002; Houze et al. 2006; Wimmers and Velden 2007). The image in Fig. 3d was obtained within 20 min prior to the first flight leg of ELDORA. Typhoon Hagupit's incipient eyewall and the predominant rainband of interest are clearly illustrated. This predominant rainband was composed of active convection that spiraled inward from the south of the

TC center and connected to the incipient eyewall north of the center. The flight track (white dashed line) of NRL P-3 indicates the region of this predominant rainband sampled by ELDORA. Figures 3a–c show additional microwave satellite images within 3 h ahead of the flight mission of ELDORA. Although there were some evolution and propagation between Figs. 3a and 3b, the same predominant rainband remained approximately at the same location relative to the TC center. The quasi-stationary characteristic of this rainband can be seen
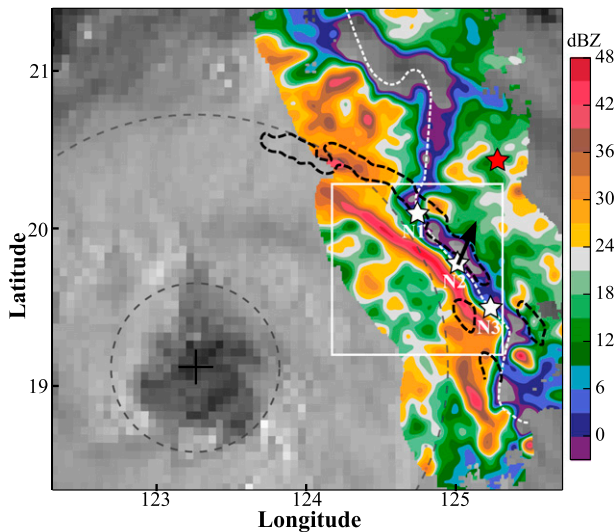
FIG. 4. Composite reflectivity field at 3-km altitude observed by ELDORA superimposed on an infrared satellite image. The white dashed line shows the flight track (flying from top to bottom) of the NRL P-3. The cross and dashed circles show the center, the RMW (60 km), and 3 times the RMW (180 km), respectively. The red (white) stars show the position of the DOTSTAR (NRL P-3) dropsonde. The black arrow on the middle white star shows the direction of low-level (0–3 km) VWS averaged from the three NRL P-3 dropsondes. The black contours show the 33-dBZ isopleths of the same convective structure observed 50 min later. The white box shows the dual-Doppler analysis domain.

more clearly in the composite animation (http://tropic.ssec.wisc.edu/real-time/mimic-tc/tc.shtml) from the Morphed Integrated Microwave Imagery (MIMIC; Wimmers and Velden 2007) product catalog.

The composite ELDORA reflectivity field at the flight level (3-km altitude) superimposed on one infrared image from the Multifunctional Transport Satellite (MTSAT) of the Japan Meteorological Agency (JMA) is shown in Fig. 4. The two dashed circles (60- and 180-km radii) indicate the RMW and 3 times the RMW from Hagupit's center. It is clear that the observed rainband was located at approximately 3 times the RMW. As will be shown in the following section, the tangential wind speed near the observed rainband is approximately $25 \, \text{m s}^{-1}$, which corresponds to a Rossby number of about 3 (Ro = v/fr, where v is the tangential wind speed, f is the Coriolis parameter, and r is the distance from the storm center; Willoughby et al. 1984; May 1996). The characteristics of this predominant rainband are consistent with the definition of the principal rainband in previous studies, including the quasi-stationary nature (Willoughby et al. 1984), the relative location with respect to the RMW (Wang 2009), geometric characteristics (Willoughby 1988; Houze 2010), and the Rossby number (Willoughby et al. 1984; May 1996).

Comparing the rainband structure shown by the satellite (Fig. 3d) and the airborne radar (Fig. 4), it is noted that only the middle portion of Hagupit's principal rainband was observed by the first flight leg. The most striking feature of Hagupit's principal rainband is the well-defined, intense convective line with continuous 40-dBZ echoes exceeding 140 km in length (Fig. 4). The convective line appears to be a discrete substructure embedded in the principal rainband compared to one continuous single band indicated by the microwave satellite image (Fig. 3d). Similar discrete convective lines (or subbanded structure) were observed for all other flight legs during this mission. This subbanded structure has been documented in previous principal rainband studies (May 1996; Hence and Houze 2008). The black dashed contours (33-dBZ isopleths) in Fig. 4 indicate the location of the same convective line observed by the second flight leg about 50 min later. The similar well-defined linear structure is clearly recognizable, which suggests that the convective line is likely a long-lived feature. Based on the averaged location of the convective line during the two flight legs, the convective line was estimated to move outward with a speed of $4.5 \, \text{m s}^{-1}$ and cyclonically with a speed of $3 \, \text{m s}^{-1}$. Although the convective line showed apparent outward and cyclonic movement, the principal rainband as a whole stayed quasi stationary with respect to the storm center as shown in Fig. 3 and the MIMIC animation. The similar structure of moving convective lines within a quasi-stationary principal rainband has been documented before (May 1996).

5. Convective structures in Hagupit's principal rainband

The linear pattern of precipitation shown in Fig. 4 is an indication of organized deep convection commonly seen in midlatitude severe convective systems (Bluestein and Jain 1985). The dual-Doppler observation from 0038 to 0102 UTC of the first flight leg, which corresponds to the dual-Doppler analysis domain in Fig. 4, was used to deduce the three-dimensional wind field of the convective line. The horizontal kinematic structures of the convective line are illustrated in Figs. 5a and 5b at 3- and 10-km altitudes, respectively. Intense convective elements with reflectivity exceeding 45 dBZ are embedded in the convective line. The dual-Doppler deduced horizontal wind speeds (white contours in Fig. 5a) at 3-km altitude decreased from about 35 to $31 \, \text{m s}^{-1}$ radially outward across the principal rainband. The dual-Doppler winds outside of the rainband are consistent with the independent aircraft in situ wind measurements (red arrows). Individual convective elements
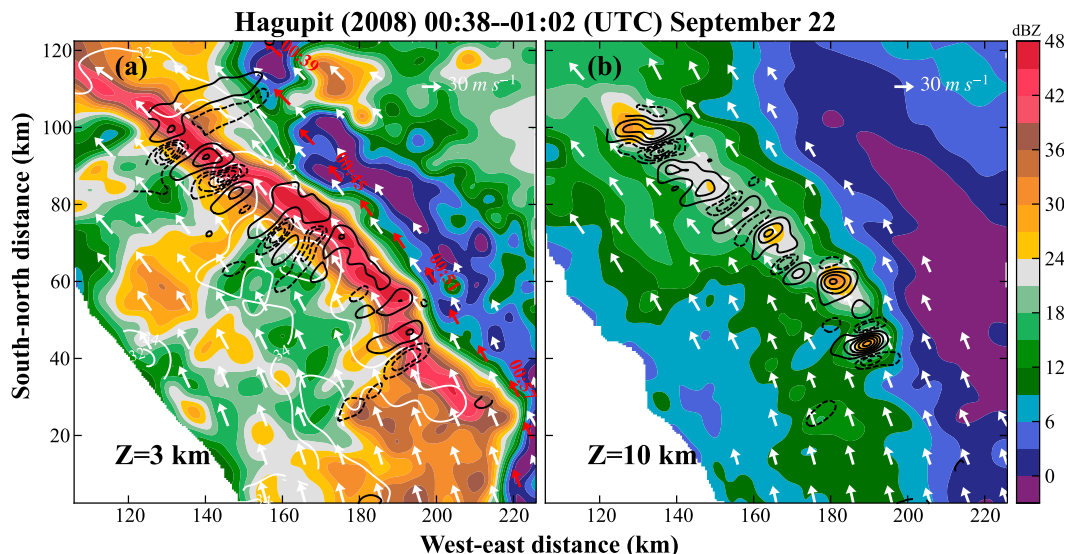
FIG. 5. Horizontal structures of Hagupit's principal rainband. (a) Kinematic and precipitation structures at 3-km altitude. White contours and arrows respectively show wind speed and wind vectors retrieved from dual-Doppler observations. Red arrows are in situ measurements by the NRL P-3. Four of them are labeled with the corresponding time (HH:MM). Black solid (dashed) contours show updrafts (downdrafts). Updrafts are shown from $2\,\mathrm{m\,s^{-1}}$ with an interval of $4\,\mathrm{m\,s^{-1}}$. Downdrafts are shown from $-2\,\mathrm{m\,s^{-1}}$ with an interval of $2\,\mathrm{m\,s^{-1}}$. (b) As in (a), but at 10-km altitude.

showed a wavelike alternating pattern with updrafts and downdrafts on spatial scales between 5 and 10 km at the 10-km altitude. A similar alternating pattern of vertical velocity was hypothesized to be a result of cell regeneration in the upwind end of TCR as the downdraft of mature cell interacted with the vortex circulation [Fig. 18 of Didlake and Houze (2009)]. These deep convective elements possessed positive vertical velocities greater than $10\,\mathrm{m\,s^{-1}}$ at 3-km altitude and $30\,\mathrm{m\,s^{-1}}$ at 10-km altitude, with negative vertical velocities less than -10 and $-14\,\mathrm{m\,s^{-1}}$, respectively. The similar magnitude of vertical velocity (updraft greater than $20\,\mathrm{m\,s^{-1}}$ and downdraft less than $-10\,\mathrm{m\,s^{-1}}$) was observed in other flight legs. Although the intense convection is consistent with the environmental conditions that will be discussed later, the extreme value of vertical velocity is still subject to the inherent uncertainties associated with the retrieval of the vertical motions from the dual-Doppler observations. The strongest updrafts tended to be located along the maximum reflectivity gradient at 3-km altitude while collocated with the reflectivity cores at 10-km altitude. A similar spatial distribution of updrafts with respect to the reflectivity field has been documented in a convective cell of Hurricane Raymond (Barnes et al. 1991). Except for the cell on the most downwind end, the updrafts associated with reflectivity cores at 10-km altitude showed a tendency for stronger vertical velocity on the upwind (south) and

weaker on the downwind (north) end, which is consistent with previous studies (Atlas et al. 1963; Houze 2010).

To better understand the structure of this intense convective line, the line-averaged vertical kinematic structure is made by averaging multiple radial–vertical cross sections (VCSs) cutting through the convective cells. Each VCS is selected through the following process. A convective–stratiform separation algorithm [appendix A of Didlake and Houze (2009)] was applied to the reflectivity field at 3-km altitude (the flight level). The separated convective regions are encompassed by the black contours superimposed on the reflectivity field in Fig. 6. It is clear that the main convective line is successfully separated from the more uniform stratiform region. Then, the axis (white dot) of the convective line was determined as the midpoint of the two convective edges along the radial direction. Using the axis as a reference, each cross section was extended 35 km inward and 25 km outward to cover a broader area associated with the convective line. The same process was repeated every 0.3° along the azimuthal direction, which corresponds to a tangential distance of approximately 1 km. The final line-averaged structure is produced by averaging each of these cross sections.

The line-averaged vertical kinematic structure is shown in Fig. 7. The 25- and 35-dBZ contours of reflectivity shown in Fig. 7a reached 9- and 6-km altitudes, respectively, which are significantly higher than those in
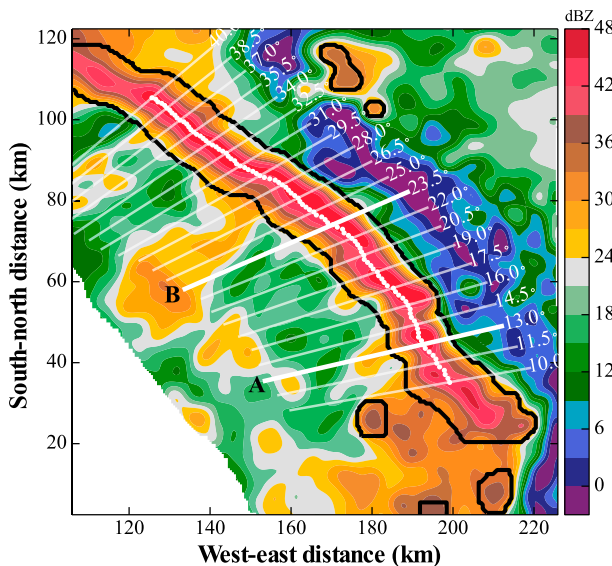
FIG. 6. Results of convective–stratiform separation algorithm and sample VCSs for producing the line-averaged vertical structure. Black contours encompass the identified convection region. White dots show the reference points on the axis of the convective line. Each dot corresponds to one VCS. White lines (drawn by every five cross sections) show the radial extent of each VCS. The numbers at the end of the lines show the azimuth of each cross section measured counterclockwise from the east. The two thick lines labeled A and B are two individual VCSs shown in Fig. 8.

previously documented principal rainbands (Barnes et al. 1983; Hence and Houze 2008). The line-averaged convective core was characterized by slightly inward-tilting reflectivity and updraft.[1] A trailing stratiform region was located radially inside of the convective line, in contrast to the sharp reflectivity gradient along the outside edge. The line-averaged updraft appears to comprise two regions. The main updraft was originated at the low level on the outer edge and reached the maximum strength greater than $4 \, \text{m s}^{-1}$ at 9-km altitude. A region of downdraft was located just radially inward of the main updraft and was likely produced by precipitation drag and evaporative cooling (Zipser 1977). Outside this main updraft region, there is a weaker updraft likely associated with newly developed cells. The line-averaged vector wind field (Fig. 7b) shows two branches of low-level inflow feeding the updraft. The first branch flowed into the convection from the outer side and turned upward with the updraft. The second branch flowed into the convection from the inner side. It is noted that part of the updraft turned

inward at mid- to high levels while the rest continued to flow upward and turned outward at the upper level. There is a strong outflow layer above 10-km altitude, and the outflow outside the convective core appears to be accelerated by the convective updraft.

Figure 8 shows two individual VCSs cutting through two active convective elements labeled in Fig. 6 as A and B. Despite individual convective cells displaying considerable variations in structure, the structures of the two VCSs are consistent with the line-averaged structure shown in Fig. 7. Both A and B showed inward-tilting reflectivity cores with stratiform precipitation inward and a sharp reflectivity gradient outward. VCS A showed a deep and upright updraft while VCS B showed an inward-tilting updraft. The two inflow branches, the midlevel inflow, and the upper-level outflow shown in the line-averaged structure can be clearly identified in the two VCSs. VCS B also showed a clear downdraft radially inside of the convective core, while VCS A was dominated by the updraft with no clear downdraft in the radial direction. The consistent structures shown in the two individual VCSs indicate that the line-averaged structure shown in Fig. 7 is representative.

The line-averaged vertical structures of Hagupit's principal rainband showed many characteristics different from previously documented TCRs. To highlight these differences, a schematic [modified based on Fig. 10 in Yu and Tsai (2013)] of Hagupit's principal rainband along with those of previously documented inner and outer TCRs is shown in Fig. 9. The vertical scale of each reflectivity boundary (10, 25, and 35 dBZ) is carefully adjusted to match recent TCR studies (Hence and Houze 2008; Didlake and Houze 2013a; Yu and Tsai 2013). As mentioned before, the existing conceptual model of a principal rainband possesses characteristics of inner TCRs with limited vertical extent and outward-tilting convective core (Fig. 9a). These characteristics indicate that the convection of inner TCRs has a strong dependence on the sheared flow associated with the vortex circulation (Rozoff et al. 2006; Wang 2008; Didlake and Houze 2013a), while the characteristics of inward-tilting convective core and the absence of upper-level outflow shown in Fig. 9b imply that the convection in outer TCRs are dominated by buoyancy instead of vortex dynamics. Hagupit's principal rainband (Fig. 9c) appears to have some characteristics of both inner and outer TCRs despite the overall structure being distinct from both of them. There is a clear outflow layer at the upper level of Hagupit's principal rainband and inner TCRs (the existing conceptual model of a principal rainband). In contrast, the precipitation structure and flow pattern are similar between Hagupit's principal rainband and
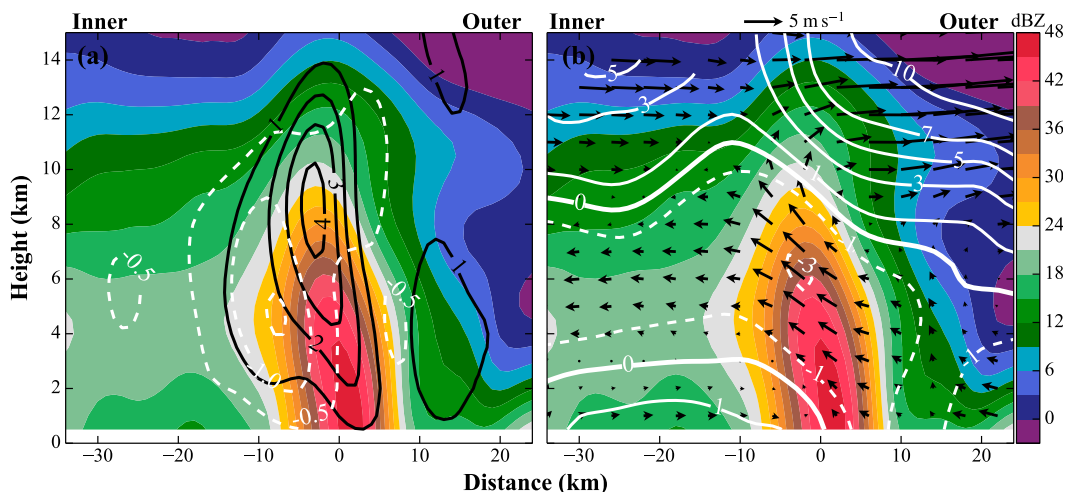
---

[1] The vertical velocity was averaged separately for the updraft and downdraft in Fig. 7a. The purpose is to prevent the downdraft from being overwhelmed by the updraft. The same technique has been used in a previous TCR study (Didlake and Houze 2009).

FIG. 7. Line-averaged vertical structures of the convection line. (a) Reflectivity (color), updraft (black; m s^{-1}), and downdraft (white contours; m s^{-1}), and (b) the wind vector (arrows) and radial velocity (white contours; m s^{-1}).

outer TCRs except for the upper-level outflow layer. The difference between Hagupit's principal rainband and outer TCRs demonstrates the potential role of storm outflow in influencing the kinematic structure of TCRs (Yu and Tsai 2013). The analysis further suggests that the natural variability of outflow at different radial distances may be important. From a pure structural perspective, it seems that Hagupit's principal rainband is in a transitional zone between inner and outer TCRs. Since the convective structures of inner and outer TCRs are manifestations of their respective dominating dynamics, the transitional characteristic of Hagupit's principal rainband implies that VWS and buoyancy may have comparable roles in determining

the unique structure of Hagupit's principal rainband. This hypothesis is further examined in the next section.

6. Mechanisms for convective line maintenance

The characteristics of line-shaped, intense, and long-lived convection in Hagupit's principal rainband are reminiscent of a squall line in the optimal state, when the convectively generated surface cold pool is quasi balanced with the environmental low-level VWS. The strength of surface cold pool is closely related to the structure, intensity of convection, and the environmental conditions. The possible role of cold pool dynamics in terms of its relation to the structure and longevity of outer
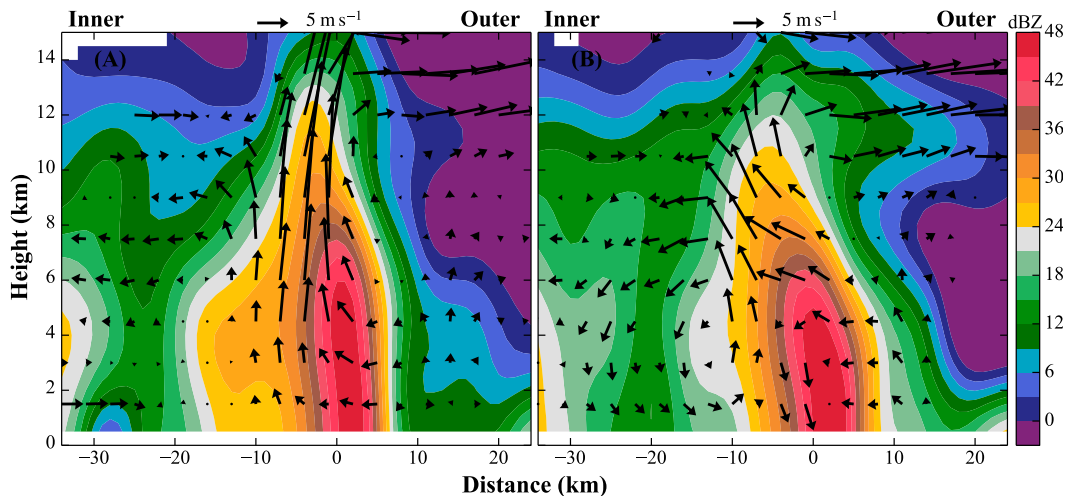

FIG. 8. Two individual VCSs labeled in Fig. 6. The label of each panel corresponds to the labels in Fig. 6. The reflectivity field is in color and the arrows are the wind vectors in the radial direction.
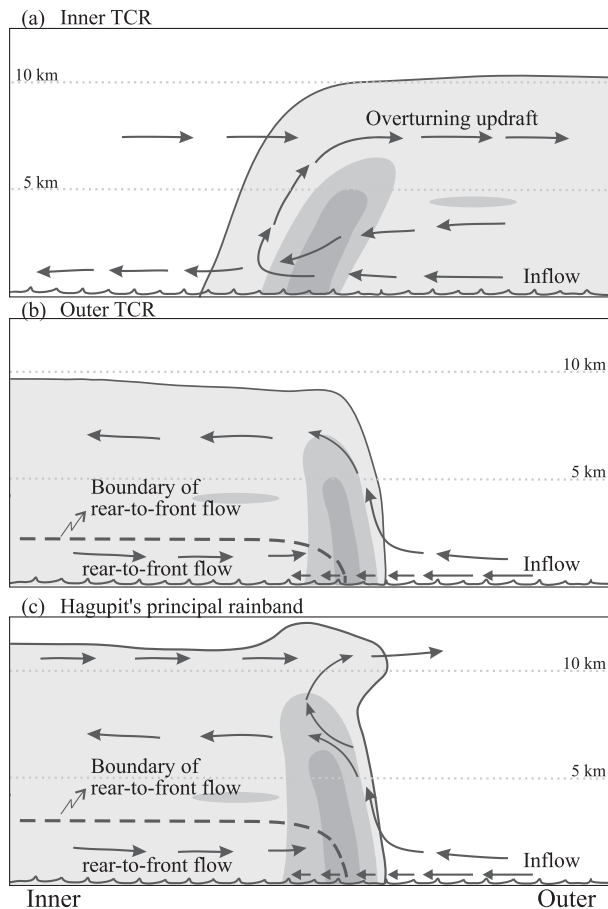
FIG. 9. A comparison of schematics [based on Yu and Tsai (2013)] of vertical structure of different rainbands. Gray colors from light to dark indicate the edges of 10, 25, and 35 dB*Z*, respectively. (a) Inner rainbands and previously documented principal rainbands. (b) Outer rainbands. (c) Hagupit's principal rainband.

FIG. 10. The skew T–log$P$ diagram and low-level hodograph of the DOTSTAR dropsonde (the red star in Fig. 4). The red (blue) line shows the temperature (dewpoint temperature) profile. The black dashed line shows the ascending path of a surface based parcel.

TCRs has been discussed in Yu and Tsai (2013). As a result of extremely weak environmental VWS (from −0.6 to 2.3 m s^{-1} in the lowest 1–3-km altitude), Yu and Tsai (2013) showed that the observed outer TCRs existed in a ''suboptimal state'' dominated by the strong cold pool. Although the ''suboptimal state'' was consistent with the inward-tilting convective cores, it was inconsistent with the long-lasting nature of the observed rainbands. As noted in previous discussions, Hagupit's principal rainband was observed over the open ocean, while the outer rainbands studied by Yu and Tsai (2013) were already near and likely influenced by the landmass of Taiwan. Bogner et al. (2000) have shown that the thermodynamic structure related to TCs can be considerably different in the open ocean from that near or over the land. Since the manifestation of the cold pool dynamics is largely determined by the environmental kinematic and thermodynamic structures, its
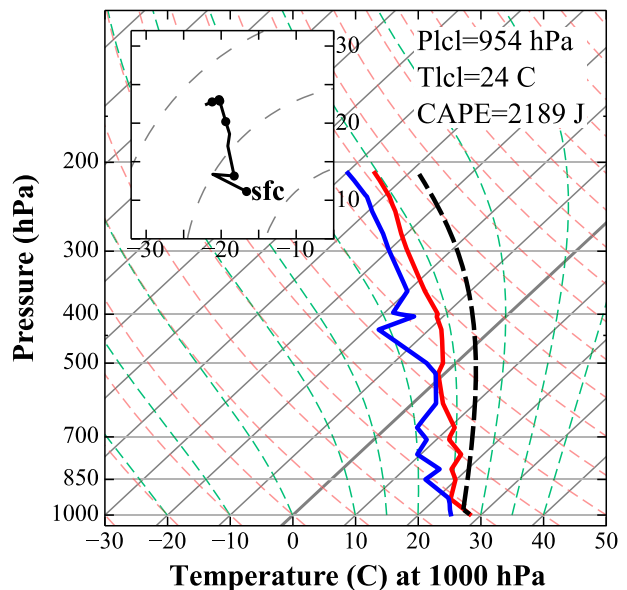
dynamic impact on TCRs in terms of the structure and evolution could also be different. To examine the applicability of cold pool dynamics in this case, the strength of the surface cold pool and low-level VWS associated with Hagupit's principal rainband were examined.

The DOTSTAR dropsonde deployed at 0012 UTC 22 September 2008 was selected to represent the environmental thermodynamic structure of Hagupit's principal rainband. As noted before, it was able to sample most of the troposphere while still spatially and temporally close to the observed rainband. The skew T–log$P$ diagram and low-level (0–3 km) hodograph of this dropsonde are shown in Fig. 10. The temperature profile was dry adiabatic up to 950 hPa and then changed to moist adiabatic above. The warm and moist air mass near the surface and the cooling above 700 hPa led to a substantial partial CAPE (up to 210 hPa or 12 km) value of 2189 J kg^{-1}. The dewpoint temperature profile showed generally unsaturated air with two moist layers at 1- and 5-km altitude and two dry layers in between 1 and 5 km and right above 5-km altitude. The large CAPE value is in favor of the development of deep convection, while the generally unsaturated condition throughout the troposphere and the enhanced dry layers are favorable for the evaporative cooling of precipitation. The hodograph from the dropsonde showed a veering low-level VWS with a magnitude of 11.2 m s^{-1} pointing to the northwest.

It is noted that the DOTSTAR dropsonde was deployed about 60 km away from the observed rainband.
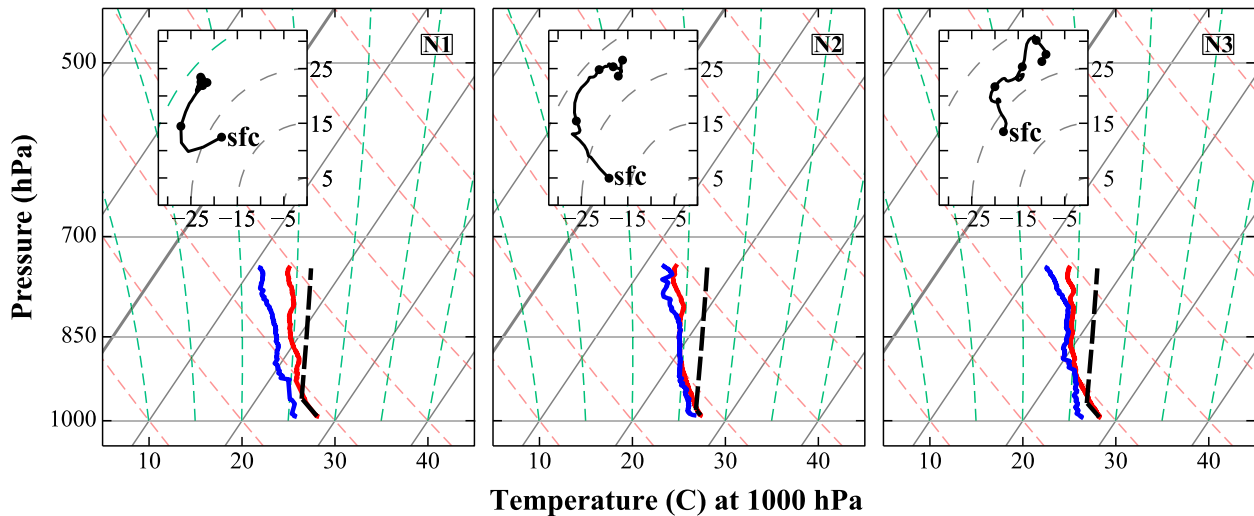
FIG. 11. As in Fig. 10, but for three NRL P-3 dropsondes (white stars in Fig. 4). The label of each panel corresponds to the labels in Fig. 4.

Since the magnitude and direction of low-level VWS in the vortex circulation strongly depend on the radial distance from the circulation center (Bogner et al. 2000), the low-level VWS shown in Fig. 10 may not be as representative as the dropsondes deployed by the NRL P-3 that were released about 10 km in front of the leading edge of the observed rainband. Figure 11 shows skew *T*–log*P* diagrams and hodographs of three NRL P-3 dropsondes deployed at the downwind (N1), middle (N2), and upwind (N3) locations of the convective line. The three hodographs all demonstrated a clear veering VWS at low levels. The low-level VWS mainly existed in the lower 2 km, which is consistent with the statistical result of low-level VWS of TCs in the Atlantic basin (Bogner et al. 2000). The direction of low-level VWS of each dropsonde was approximately perpendicular to the orientation of the convective line at the appropriate azimuthal location. The averaged magnitude and direction of low-level VWS of the three dropsondes is about 14.8 m s^{-1} pointing toward about 30° clockwise from the north (black arrow in Fig. 4). Only the thermodynamic structure in the portion below 700 hPa was observed by the NRL P-3 dropsondes, but the three dropsondes showed consistent characteristics with the DOTSTAR dropsonde, including the dry adiabatic temperature profile near the surface and the enhanced moist (dry) layer at 925 (850–750) hPa.

The values of CAPE and low-level VWS in the environment of Hagupit's principal rainband are considerably stronger than those of previous observational studies (Barnes et al. 1991; May 1996; Yu and Tsai 2013). Except for the intrinsic spatial variation of these values inside a TC, the difference could also result from the different ways of assessing the magnitude of the two

variables. Barnes et al. (1991) used descending and ascending flight in situ observations to synthesize an environmental sounding. This technique suffers from large spatial and temporal smoothing. May (1996) used soundings launched within the rainband and velocity azimuthal display (VAD)-based wind profiles to characterize the thermodynamic and kinematic structures of the rainband's environment. It is likely that the environment was modified by the convection associated with the rainband, however. Yu and Tsai (2013) used dual-Doppler retrieved wind field in front of the rainband to characterize its low-level VWS. This technique is also limited to the accuracy of the retrieved wind field. The availability of both NRL P-3 and DOTSTAR dropsondes provided an ideal condition to investigate the environment of Hagupit's principal rainband. In addition, the CAPE and low-level VWS are only marginally greater than their maximum values collected by dropsondes in the Atlantic Ocean (Bogner et al. 2000). As shown by RKW, the existence of considerable CAPE and VWS is necessary for the manifestation of cold pool dynamics. The corresponding bulk Richardson number is approximately 20, which is favorable for long-lived convection (Weisman and Klemp 1982).

The large CAPE value and generally unsaturated troposphere are favorable for the evaporative cooling process and, subsequently, the formation of a surface cold pool. The direct assessment of the cold pool structure is made possible by the retrieved virtual cloud potential temperature perturbations (Roux et al. 1993) using the reflectivity and three-dimensional wind field. The line-averaged structure of retrieved virtual cloud potential temperature perturbations calculated in the same way as that of the kinematic structure (Fig. 7) is illustrated
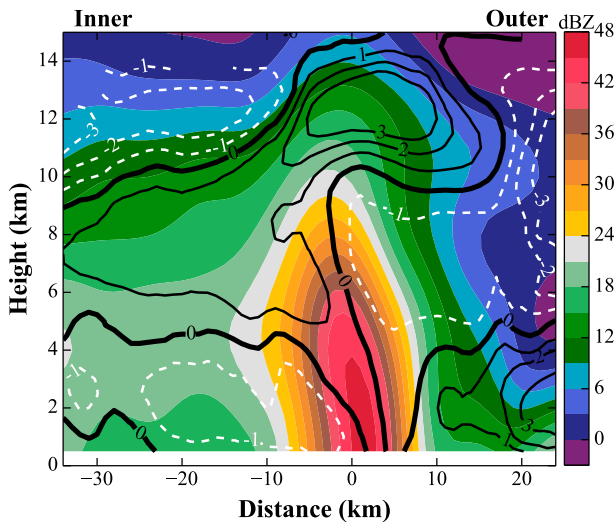
FIG. 12. Line-averaged temperature perturbation (K) superimposed on the reflectivity field (color).

in Fig. 12. The perturbation field directly computed from the retrieval algorithm is relative to an environmental sounding. In this case, the DOTSTAR dropsonde (red star in Fig. 4) was used as the environmental sounding. To better capture the local perturbation relative to the convection rather than the reference dropsonde, the averages of each vertical level were subtracted from the retrieved perturbation field before producing the line-averaged structure (Didlake and Houze 2009). The perturbation field in Fig. 12 showed a positive anomaly associated with the main updraft core in Fig. 7a. Radially inside the positive anomaly and in the stratiform region, a cold pool with a negative temperature perturbation less than -1 K extended from the lowest analysis level to around 4 km. It was likely the result of evaporative cooling of precipitation. The magnitude and vertical extent of this cold pool signature are comparable with previous observations (Yu and Chen 2011; Eastin et al. 2012). Following RKW, the averaged strength of the cold pool was estimated by

$$ C = \sqrt{g \frac{\Delta \theta_v}{\theta_{v0}} H}, $$

where g is the gravitational acceleration, θ_{v0} is the base-state virtual potential temperature, $\Delta \theta_v$ is the virtual potential temperature perturbation of the cold pool relative to the environment,[2] and H is the average cold

pool depth; θ_{v0} is estimated to be about 305 K using the DOTSTAR dropsonde profile in Fig. 10, and $\Delta \theta_v$ and H were estimated from the retrieved temperature perturbations. Based on Fig. 12, H was estimated to be 3 km by the averaged depth of the negative temperature perturbation region and $\Delta \theta_v$ was about 3 K between the front and rear sides of the convection. These values lead to an estimated cold pool strength C of approximately $17.0 \, \text{m s}^{-1}$. The relative strength of the cold pool and low-level VWS are close to the balanced (or optimal) state that is most ideal for strong and long-lived squall lines (RKW). The stronger cold pool strength is consistent with the slightly inward-tilting convective core. The balanced state and the structural similarity to strong and long-lived squall lines indicate that the cold pool dynamics may play an important role in determining the principal rainband structure in addition to vortex dynamics.

7. Summary and conclusions

In this study, the structure of Typhoon Hagupit's principal rainband was investigated using high-resolution ELDORA observations from NRL P-3 and dropsonde observations from DOTSTAR. While the existing conceptual model of a principal rainband appears to have characteristics associated with inner rainbands, Hagupit's principal rainband shows many characteristics associated with both inner and outer rainbands. A 140-km long, intense, and well-defined convective line segment was observed in this principal rainband. The individual convective cells possessed deep and intense updrafts. The alternating updraft and downdraft structures along the convective line resembled a wavelike pattern. The line-averaged vertical convective structure tilted slightly radially inward toward the trailing stratiform region. Two updraft cores were associated with the mature and new cells. The cross-band flow showed two inflow branches feeding the main updraft from both inside and outside. One aspect in which the Hagupit principal rainband resembles an inner rainband is that the updraft merged with the high-level outflow away from the TC center, indicating that the storm-scale secondary circulation is still important in this region. The intensity and flow pattern of convection in Hagupit's principal rainband is reminiscent of a long-lived squall line in its mature stage. The observed convective line was accompanied by considerable low-level VWS and CAPE. The derived bulk Richardson number of about 20 indicated a favorable environment for the development of long-lived convection. Temperature retrievals indicated that the line-averaged updraft core had a positive temperature perturbation and that a cold pool with a maximum temperature difference of

---

[2] The retrieved perturbation field includes the contribution from cloud particles. Since the cold pool is usually located under the cloud base, the cloud contribution to the temperature difference of cold pool is negligible.

3 K and an average height of 3 km was located behind the convective line.

The convective structure in Hagupit's principal rainband is consistent with an approximate balance between the negative horizontal vorticity from the local low-level VWS and the positive horizontal vorticity from the cold pool. The low-level VWS was nearly perpendicular to the principal rainband with a magnitude of about $14.8 \, \text{m s}^{-1}$, similar to the estimated magnitude of cold pool strength of $17.0 \, \text{m s}^{-1}$. The slight inward tilt is consistent with stronger cold pool strength. The dynamic and structural similarities with squall lines suggest that the cold pool dynamics is applicable in explaining the convective structure of Hagupit's principal rainband and that cold pool and low-level VWS interaction may have played an important role in addition to storm-scale vortex dynamics. The squall-line-like mechanism for intense and long-lived convection may have also impacted the intensity of the typhoon by increasing the associated vortex stretching and diabatic heating in Hagupit's principal rainband. Further research is necessary to better understand the role of this unique principal rainband during Hagupit's intensifying stage.

REFERENCES

Atlas, D., K. R. Hardy, R. Wexler, and R. J. Boucher, 1963: On the origin of hurricane spiral bands. *Geofis. Int.,* **3,** 123–132.

Barnes, G. M., E. J. Zipser, D. P. Jorgensen, and F. D. Marks, 1983: Mesoscale and convective structure of a hurricane rainband. *J. Atmos. Sci.,* **40,** 2125–2137, doi:10.1175/1520-0469(1983)040<2125:MACSOA>2.0.CO;2.

——, M. A. LeMone, G. J. Stossmeister, and J. F. Gamache, 1991: A convective cell in a hurricane rainband. *Mon. Wea. Rev.,* **119,** 776–794, doi:10.1175/1520-0493(1991)119<0776:ACCIAH>2.0.CO;2.

Bell, M. M., and M. T. Montgomery, 2010: Sheared deep vortical convection in pre-depression Hagupit during TCS08. *Geophys. Res. Lett.,* **37,** L06802, doi:10.1029/2009GL042313.

——, W.-C. Lee, C. A. Wolff, and H. Cai, 2013: A solo-based automated quality control algorithm for airborne tail Doppler radar data. *J. Appl. Meteor. Climatol.,* **52,** 2509–2528, doi:10.1175/JAMC-D-12-0283.1.

Bluestein, H. B., and M. H. Jain, 1985: Formation of mesoscale lines of precipitation: Severe squall lines in Oklahoma during the spring. *J. Atmos. Sci.,* **42,** 1711–1732, doi:10.1175/1520-0469(1985)042<1711:FOMLOP>2.0.CO;2.

——, G. T. Marx, and M. H. Jain, 1987: Formation of mesoscale lines of precipitation: Nonsevere squall lines in Oklahoma during the spring. *Mon. Wea. Rev.,* **115,** 2719–2727, doi:10.1175/1520-0493(1987)115<2719:FOMLOP>2.0.CO;2.

Bogner, P., G. Barnes, and J. Franklin, 2000: Conditional instability and shear for six hurricanes over the Atlantic Ocean. *Wea. Forecasting,* **15,** 192–207, doi:10.1175/1520-0434(2000)015<0192:CIASFS>2.0.CO;2.

Bosart, B. L., W.-C. Lee, and R. M. Wakimoto, 2002: Procedures to improve the accuracy of airborne Doppler radar data. *J. Atmos. Oceanic Technol.,* **19,** 322–339, doi:10.1175/1520-0426-19.3.322.

Chou, K.-H., C.-C. Wu, P.-H. Lin, S. D. Aberson, M. Weissmann, F. Harnisch, and T. Nakazawa, 2011: The impact of dropwindsonde observations on typhoon track forecasts in DOTSTAR and T-PARC. *Mon. Wea. Rev.,* **139,** 1728–1743, doi:10.1175/2010MWR3582.1.

Didlake, A. C., and R. A. Houze, 2009: Convective-scale downdrafts in the principal rainband of Hurricane Katrina (2005). *Mon. Wea. Rev.,* **137,** 3269–3293, doi:10.1175/2009MWR2827.1.

——, and ——, 2013a: Convective-scale variations in the inner-core rainbands of a tropical cyclone. *J. Atmos. Sci.,* **70,** 504–523, doi:10.1175/JAS-D-12-0134.1.

——, and ——, 2013b: Dynamics of the stratiform sector of a tropical cyclone rainband. *J. Atmos. Sci.,* **70,** 1891–1911, doi:10.1175/JAS-D-12-0245.1.

Eastin, M. D., T. L. Gardner, M. C. Link, and K. C. Smith, 2012: Surface cold pools in the outer rainbands of Tropical Storm Hanna (2008) near landfall. *Mon. Wea. Rev.,* **140,** 471–491, doi:10.1175/MWR-D-11-00099.1.

Elsberry, R. L., and P. A. Harr, 2008: Tropical Cyclone Structure (TCS08) field experiment science basis, observational platforms, and strategy. *Asia-Pac. J. Atmos. Sci.,* **44,** 209–231.

Gamache, J. F., 1997: Evaluation of a fully-three dimensional variational Doppler analysis technique. Preprints, *28th Conf. on Radar Meteorology,* Austin, TX, Amer. Meteor. Soc., 422–423.

Hence, D. A., and R. A. Houze Jr., 2008: Kinematic structure of convective-scale elements in the rainbands of Hurricanes Katrina and Rita (2005). *J. Geophys. Res.,* **113,** D15108, doi:10.1029/2007JD009429.

Hildebrand, P. H., and Coauthors, 1996: The ELDORA/ASTRAIA airborne Doppler weather radar: High-resolution observations from TOGA COARE. *Bull. Amer. Meteor. Soc.,* **77,** 213–232, doi:10.1175/1520-0477(1996)077<0213:TEADWR>2.0.CO;2.

Houze, R. A., Jr., 2010: Clouds in tropical cyclones. *Mon. Wea. Rev.,* **138,** 293–344, doi:10.1175/2009MWR2989.1.

——, and Coauthors, 2006: The hurricane rainband and intensity change experiment: Observations and modeling of Hurricanes Katrina, Ophelia, and Rita. *Bull. Amer. Meteor. Soc.,* **87,** 1503–1521, doi:10.1175/BAMS-87-11-1503.

——, S. S. Chen, B. F. Smull, W.-C. Lee, and M. M. Bell, 2007: Hurricane intensity and eyewall replacement. *Science,* **315,** 1235–1239, doi:10.1126/science.1135650.

——, W.-C. Lee, and M. M. Bell, 2009: Convective contribution to the genesis of Hurricane Ophelia (2005). *Mon. Wea. Rev.,* **137,** 2778–2800, doi:10.1175/2009MWR2727.1.

Lee, T. F., F. J. Turk, J. Hawkins, and K. Richardson, 2002: Interpretation of TRMM TMI images of tropical cyclones. *Earth Interact.,* **6,** doi:10.1175/1087-3562(2002)006<0001:IOTTIO>2.0.CO;2.

Leise, J. A., 1981: A multidimensional scale-telescoped filter and data extension package. NOAA Tech. Memo. ERL WPL-82, 20 pp.

Li, Q., and Y. Wang, 2012: A comparison of inner and outer spiral rainbands in a numerically simulated tropical cyclone. *Mon. Wea. Rev.,* **140,** 2782–2805, doi:10.1175/MWR-D-11-00237.1.

May, P. T., 1996: The organization of convection in the rainbands of Tropical Cyclone Laurence. *Mon. Wea. Rev.,* **124,** 807–815, doi:10.1175/1520-0493(1996)124<0807:TOOCIT>2.0.CO;2.

Molinari, J., D. M. Romps, D. Vollaro, and L. Nguyen, 2012: CAPE in tropical cyclones. *J. Atmos. Sci.,* **69,** 2452–2463, doi:10.1175/JAS-D-11-0254.1.

Oye, R., C. Mueller, and S. Smith, 1995: Software for radar translation, visualization, editing, and interpolation. Preprints, *27th Conf. on Radar Meteorology,* Vail, CO, Amer. Meteor. Soc., 359–361.

Powell, M. D., 1990: Boundary layer structure and dynamics in outer hurricane rainbands. Part II: Downdraft modification and mixed layer recovery. *Mon. Wea. Rev.,* **118,** 918–938, doi:10.1175/1520-0493(1990)118<0918:BLSADI>2.0.CO;2.

Reasor, P. D., M. T. Montgomery, F. D. Marks, and J. F. Gamache, 2000: Low-wavenumber structure and evolution of the hurricane inner core observed by airborne dual-Doppler radar. *Mon. Wea. Rev.,* **128,** 1653–1680, doi:10.1175/1520-0493(2000)128<1653:LWSAEO>2.0.CO;2.

——, M. D. Eastin, and J. F. Gamache, 2009: Rapidly intensifying Hurricane Guillermo (1997). Part I: Low-wavenumber structure and evolution. *Mon. Wea. Rev.,* **137,** 603–631, doi:10.1175/2008MWR2487.1.

Rogers, R. F., S. Lorsolo, P. D. Reasor, J. F. Gamache, and F. D. Marks, 2012: Multiscale analysis of tropical cyclone kinematic structure from airborne Doppler radar composites. *Mon. Wea. Rev.,* **140,** 77–99, doi:10.1175/MWR-D-10-05075.1.

Rotunno, R., J. B. Klemp, and M. L. Weisman, 1988: A theory for strong long-lived squall lines. *J. Atmos. Sci.,* **45,** 463–485, doi:10.1175/1520-0469(1988)045<0463:ATFSLL>2.0.CO;2.

Roux, F., V. Marécal, and D. Hauser, 1993: The 12/13 January 1988 narrow cold-frontal rainband observed during MFDP/FRONTS 87. Part I: Kinematics and thermodynamics. *J. Atmos. Sci.,* **50,** 951–974, doi:10.1175/1520-0469(1993)050<0951:TJNCFR>2.0.CO;2.

Rozoff, C. M., W. H. Schubert, B. D. McNoldy, and J. P. Kossin, 2006: Rapid filamentation zones in intense tropical cyclones. *J. Atmos. Sci.,* **63,** 325–340, doi:10.1175/JAS3595.1.

Sawada, M., and T. Iwasaki, 2010: Impacts of evaporation from raindrops on tropical cyclones. Part II: Features of rainbands and asymmetric structure. *J. Atmos. Sci.,* **67,** 84–96, doi:10.1175/2009JAS3195.1.

Sheets, R. C., 1969: Some mean hurricane soundings. *J. Appl. Meteor.,* **8,** 134–146, doi:10.1175/1520-0450(1969)008<0134:SMHS>2.0.CO;2.

Simpson, R., R. Anthes, M. Garstang, and J. Simpson, 2003: *Hurricane! Coping with Disaster: Progress and Challenges since Galveston, 1900.* Amer. Geophys. Union, 360 pp.

Skwira, G. D., J. L. Schroeder, and R. E. Peterson, 2005: Surface observations of landfalling hurricane rainbands. *Mon. Wea. Rev.,* **133,** 454–465, doi:10.1175/MWR-2866.1.

Spencer, R. W., H. M. Goodman, and R. E. Hood, 1989: Precipitation retrieval over land and ocean with the SSM/I: Identification and characteristics of the scattering signal. *J. Atmos. Oceanic Technol.,* **6,** 254–273, doi:10.1175/1520-0426(1989)006<0254:PROLAO>2.0.CO;2.

Testud, J., P. H. Hildebrand, and W.-C. Lee, 1995: A procedure to correct airborne Doppler radar data for navigation errors using the echo returned from the earth's surface. *J. Atmos. Oceanic Technol.,* **12,** 800–820, doi:10.1175/1520-0426(1995)012<0800:APTCAD>2.0.CO;2.

Wang, Y., 2008: Rapid filamentation zone in a numerically simulated tropical cyclone. *J. Atmos. Sci.,* **65,** 1158–1181, doi:10.1175/2007JAS2426.1.

——, 2009: How do outer spiral rainbands affect tropical cyclone structure and intensity? *J. Atmos. Sci.,* **66,** 1250–1273, doi:10.1175/2008JAS2737.1.

Weisman, M. L., and J. B. Klemp, 1982: The dependence of numerically simulated convective storms on vertical wind shear and buoyancy. *Mon. Wea. Rev.,* **110,** 504–520, doi:10.1175/1520-0493(1982)110<0504:TDONSC>2.0.CO;2.

——, and R. Rotunno, 2004: A theory for strong long-lived squall lines revisited. *J. Atmos. Sci.,* **61,** 361–382, doi:10.1175/1520-0469(2004)061<0361:ATFSLS>2.0.CO;2.

Willoughby, H. E., 1988: The dynamics of the tropical cyclone core. *Aust. Meteor. Mag.,* **36,** 183–191.

——, F. D. Marks, and R. Feinberg, 1984: Stationary and moving convective bands in hurricanes. *J. Atmos. Sci.,* **41,** 3189–3211, doi:10.1175/1520-0469(1984)041<3189:SAMCBI>2.0.CO;2.

Wimmers, A. J., and C. S. Velden, 2007: MIMIC: A new approach to visualizing satellite microwave imagery of tropical cyclones. *Bull. Amer. Meteor. Soc.,* **88,** 1187–1196, doi:10.1175/BAMS-88-8-1187.

Wu, C.-C., and Coauthors, 2005: Dropwindsonde Observations for Typhoon Surveillance near the Taiwan Region (DOTSTAR): An overview. *Bull. Amer. Meteor. Soc.,* **86,** 787–790, doi:10.1175/BAMS-86-6-787.

Yu, C.-K., and C.-L. Tsai, 2010: Surface pressure features of landfalling typhoon rainbands and their possible causes. *J. Atmos. Sci.,* **67,** 2893–2911, doi:10.1175/2010JAS3312.1.

——, and Y. Chen, 2011: Surface fluctuations associated with tropical cyclone rainbands observed near Taiwan during 2000–08. *J. Atmos. Sci.,* **68,** 1568–1585, doi:10.1175/2011JAS3725.1.

——, and C.-L. Tsai, 2013: Structural and surface features of arc-shaped radar echoes along an outer tropical cyclone rainband. *J. Atmos. Sci.,* **70,** 56–72, doi:10.1175/JAS-D-12-090.1.

Zipser, E. J., 1977: Mesoscale and convective-scale downdrafts as distinct components of squall-line structure. *Mon. Wea. Rev.,* **105,** 1568–1589, doi:10.1175/1520-0493(1977)105<1568:MACDAD>2.0.CO;2.